RESEARCH ARTICLE | OCTOBER 01 2024

Flow field characteristics and vibration responses of saddle-shaped membrane structures

Special Collection: Flow and Civil Structures

Dong Li ; Renyang Shen; Qiyin Zhu; Leiyu Lu; Hao Ding ; Xiaoqiang Yang

Physics of Fluids 36, 107106 (2024)
https://doi.org/10.1063/5.0230419

Physics of Fluids ARTICLE pubs.aip.org/aip/pof

Flow field characteristics and vibration responses of saddle-shaped membrane structures

Cite as: Phys. Fluids **36**, 107106 (2024); doi: 10.1063/5.0230419
Submitted: 23 July 2024 · Accepted: 13 September 2024 ·
Published Online: 1 October 2024

Dong Li,[1,2] Renyang Shen,[1] Qiyin Zhu,[1] Leiyu Lu,[1] Hao Ding,[3] and Xiaoqiang Yang[3,a)]

AFFILIATIONS

[1]College of Civil Engineering, Fuzhou University, Fuzhou 350116, China
[2]Key Laboratory of Fluid and Power Machinery, Ministry of Education, Xihua University, Chengdu 610039, China
[3]Department of Civil and Environmental Engineering, The Hong Kong Polytechnic University, Hung Hom, Kowloon, Hong Kong 999077, China

Note: This paper is part of the special topic, Flow and Civil Structures.
[a)]**Author to whom correspondence should be addressed:** xiaoqiang.yang@polyu.edu.hk

ABSTRACT

Elastically mounted flexible membrane roofs exposed to flows are prone to vortex-induced vibrations and even aero-instability due to the strong fluid–structure interaction (FSI). This study is to investigate the FSI mechanism in the saddle-shaped membrane structure over a range of Reynolds numbers and wind directions in laminar flows, by bridging structural vibration responses and flow dynamics. The aeroelastic characteristics of membrane structures, including statistics of displacement responses, oscillation frequency, and oscillation damping ratios, were identified from the perspective of time and frequency domains. Simultaneously, the particle image velocimetry system was employed to visualize the flow features, including velocity vector, turbulence intensity, and vortex evolution in both space and time. The flow modes were further decomposed by proper orthogonal decomposition (POD) to capture the salient aspects of the flow. Three patterns of POD modes are identified, and the first mode plays the dominant role in POD modes. It showed that as the wind Reynolds number increases, the space between the shear layer and membrane surface would be narrowed, and resultantly the vortices turn out smaller in scale and closer in space. This trend leads to an increase in the frequency of vortex shedding and a stronger FSI effect. When the frequency of vortex shedding approaches the fundamental frequency of structures, the vibration of the membrane would be shifted from turbulent buffeting to vortex-induced resonance, featured with lock-in frequency, significant amplified displacement, and negative aerodynamic damping ratio.

I. INTRODUCTION

Membrane structures, as a type of flexible roof, are highly sensitive to wind loading, along with a series of aeroelastic phenomena such as buffeting, aeroelastic instability, and potential structural damage.[1–3] Wind-induced vibration issues of flexible membrane structures generally exist in their service life cycle, which can be categorized into three types of vibration mechanisms, including motion-induced vibration (MIV) caused by the structure's motion, externally-induced vibration (EIV) induced by external wind loads, and coupled vibration (MIV–EIV). MIV is the vibration caused by the properties of the membrane structure itself. This vibration is usually related to the mass, stiffness, damping and acceleration of the membrane structure. EIV is the vibration of the membrane structure usually caused by the excitation of external wind field. Due to their lightweight and flexible nature, membrane structures are prone to significant deformations when subjected to the combined effects of MIV and EIV. Such deformations alter the geometric shape and surface characteristics of the membrane, thereby changing the boundary conditions of the flow field and leading to variations in fluid dynamic properties (e.g., velocity and pressure distribution). When the combined effects of MIV and EIV meet specific conditions, they can induce strong fluid structure interaction (FSI) effects between the membrane structure and the flow field.[4,5] The FSI refers to the phenomenon between the flexible structure and the fluid surrounding the structure. Specifically, the flexible structure is prone to flow-induced large deformations with strong geometrical nonlinearity, and in turn, the fluid pattern would be developed further as well as the varying wind pressure on a deformable structure. Consequently, the repetitive interaction process would enlarge the dynamic response and lead to the aero-instability and failure of stationary structures in the stationary fluid. Thus, it is necessary to fully understand the FSI mechanism in view of wind-resistant design.

In past decades, researchers have investigated the FSI mechanism of two-dimensional (2D) membranes through experimental studies and numerical simulations. They have demonstrated that the vortices that formed originally on stationary models can be the aerodynamic excitation of membrane structures, and would be greatly amplified by structural deformations.[6–8] Tregidgo *et al.*[10] and Rojratsirikul *et al.*[9] indicated that the vibration of the two-dimensional airfoil was closely associated with the development of the shear layer, by using the particle image velocimetry (PIV) technology to visualize the flow field. Furthermore, the scale of the laminar separation bubble can affect the vibration response of flexible airfoils, and even change the vibration mode from multi-mode into single-mode.[11,12] Yu *et al.*[13] indicated that with increasing wind velocity, the surrounding fluid can enlarge the effective mass of the structure, and further amplify the vibration response. Gordnier[14] found that increasing membrane stiffness or reducing membrane tension may make the flow unstable and decrease the frequency of vortex shedding. The distribution of mean wind pressure coefficients was depended on the conditions of vortex shedding and reattachment.[15] Takadate and Uematsu[16] used forced vibration simulation methods to calculate the unsteady aerodynamic forces affected by membrane vibration frequency. Yang *et al.*[17,18] revealed that the aero-elastic instability occurred with the phenomenon of the mode jump and negative aerodynamic damping.

Recently, the FSI mechanism of three-dimensional (3D) membrane structures has been paid more attention, with more intricate interaction between the flow features and structural dynamic properties. Liu *et al.*[19] studied the galloping problem of tension orthotropic saddle shaped closed membrane structures and concluded that the span ratio, pretension, and amplitude of the membrane structure would affect the critical wind speed. Rasim *et al.*[20] and Wang *et al.*[21] considered the effects of FSI in constitutive relations when establishing theoretical models. Liu *et al.*[22] developed a theoretical model which can effectively predict the random vibration characteristics of membrane structures under wind load and calculate the reliability index of membrane structures. To take the FSI into consideration numerically, Glück *et al.*[23] and Alexander *et al.*[24] proposed a fully coupled numerical model of pre-stressed textile roofs by integrating computational fluid dynamics (CFD) and computational structure dynamics (CSD) techniques. The FSI simulation methodology proposed has been proven to be available and possible in practical complex structural design. Wang *et al.*[25] indicated that aerodynamic damping had a nonlinear relationship with vibration amplitude through numerical analysis of wrinkled membranes. Yang *et al.*[26] numerically proposed the nonlinear model of the motion-induced aerodynamic forces on large-scale hyperbolic paraboloid membranes. In wind tunnel tests, Kandel *et al.*[27] investigated the pressure distribution of rectangular-shaped arch-supported membrane structures, and found that strong flow separation occurred in the windward arch edge which resulted in larger suction pressure. Li *et al.*[28] found that larger wind velocities and higher turbulence intensity were more unfavorable to the structural dynamic response, featured by larger vibration statistics and smaller damping ratios. Liu *et al.*[29] found that cord tension relaxation or weak boundary conditions can significantly affect the stiffness of membrane structures, finally reducing its critical wind speed. Wood *et al.*[30] and Wu *et al.*[31] observed that there existed two different patterns of structural aeroelastic response, namely turbulent buffeting and aeroelastic instability. These two distinct patterns were influenced by various parameters, including wind velocities, internal pressures, and membrane tensile stiffness.

In summary, it was shown that the topic of FSI of flexible membrane structures was highly associated with the wind-resistant design of building roofs. Various methods have been developed to characterize the FSI effect between the deformable membrane structure and the flow field experimentally, numerically, and theoretically. The FSI mechanism was revealed in various views, involving visualizing the vortex characteristics in flow fields, measuring the wind speed and frequency spectrum, identifying the surface pressure coefficients of rigid membrane models, and investigating the aeroelastic response of flexible membrane models. However, these characteristics are independently considered and discussed in addressing FSI issues. Thus, there is still a lack of systematic experimental study and fundamental test data to reveal the coherent relations of 3D flexible membrane structures between flow field and structural aeroelastic response, especially with respect to the saddle-shaped membrane structures typically used in engineering.

To fill the gap, this paper systematically investigated the FSI mechanism of a saddle-shaped membrane structure. A scaled model is designed and tested in laminar flows simulated in wind tunnels to investigate the aero-elastic characteristics of membrane structures, including displacement statistics, frequency, damping ratio, *etc.* Subsequently, the flow features including velocity, Reynolds numbers, turbulence intensity, and vortex evolution are visualized using the PIV technique, and the flow field modes are further extracted by the orthogonal decomposition (POD) method. Finally, the FSI mechanism of the membrane structure can be revealed in terms of both the flow field and vibration responses. Then, the critical wind and aero-instability mechanism can be identified.

II. EXPERIMENTAL STUDY

A. Design of scaled model

The wind tunnel test of the scaled membrane structure model was designed based on the scaling criteria, including geometric, aerodynamic, and stiffness similarities.[32] Table I summarizes the conversion relationship between the scaled model and the prototype. Among the aerodynamic similarity, the Froude number between scaled model and its prototype should be identical. Then, the relationship between the geometrical scale λ_L and the flow velocity scale λ_V can be obtained, i.e., $\lambda_L = \lambda 2$ V. The prototype geometry of the membrane structures is a hyperbolic paraboloid with the $4 \times 4\,m^2$ rectangular plan and 0.3 m sag/0.55 m rise. The geometrical scale is selected as $\lambda_L = 1/10$, and the flow velocity scale is derived as $\lambda_V = 1/\sqrt{10}$. Consequently, the dimension of the scaled model is $400 \times 400\,mm^2$, and the heights are 30 mm

TABLE I. Conversion relationship between model and prototype.

Parameter	Dimension	Scale relation	Scale ratio
Length	L	λ_L	1/10
Velocity	$L^{1/2}$	$\lambda_L^{1/2}$	$1/\sqrt{10}$
Area	L^2	λ_L^2	1/100
Time	T	$\lambda_V^{-1}\lambda_L$	$1/\sqrt{10}$
Frequency	T^{-1}	$\lambda_V\lambda_L^{-1}$	$\sqrt{10}$
Equivalent elastic modulus	$L^{-1}MT^{-2}$	λ_V^2	1/10

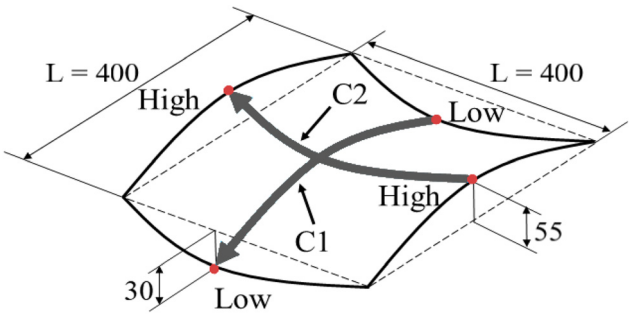

FIG. 1. Schematic diagram of model.

TABLE II. Technical parameters of materials.

Technical parameter	Unit	Value
Yield stress	MPa	>22
Thermal conductivity	W/m°C	0.25
Linear thermal expansion	mm/m°C	0.9
Area density	g/m^2	437
Total thickness	mm	0.25
Elastic modulus	MPa	800
Tensile strength (machine direction)	MPa	>50
Tensile strength (transverse direction)	MPa	>50

sag/55 mm rise, as shown in Fig. 1, where C1 and C2 refer to the convex and concave curvature, respectively.

The membrane material was selected from an ethylene tetra fluoro ethylene (ETFE) sheet, with the thickness of $t = 0.25$ mm, the Young's modulus of $E = 800$ MPa, and the surface density of $\rho = 437$ g/cm^2. Table II lists the material parameters of the membrane used in the experiment. The investigated membrane was pre-tensioned and elastically mounted onto a steel frame, as shown in Fig. 2.

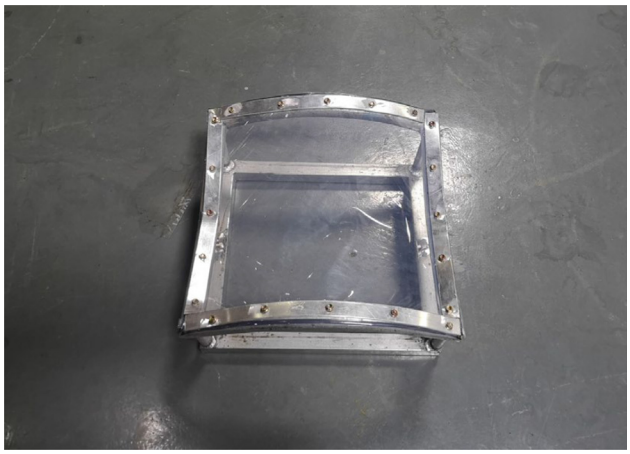

FIG. 2. Photograph of model.

B. Experimental setup and measuring techniques

1. Experimental setups

The experiment was conducted in the wind tunnel of the Key Laboratory of Fluid and Power Machinery of the Ministry of Education at Xihua University. Figure 3 shows the schematic diagram of wind tunnel experiments. The low-speed tunnel is featured with a test section of approximately 1200×1200 mm^2, a length of 3000 mm, and a maximum wind speed of 60 m/s. The desired wind field can be simulated by the wind tunnel control system. A comprehensive understanding of FSI mechanisms need to consider both fluid and structure measurements. In this test, the velocity field of flows is captured by a 2D PIV setup, and the structural vibrations are measured by the laser sensors. High temporal and spatial resolution and low measurement errors can be achieved by the following measuring techniques. The schematic diagram of the experiment is illustrated in Fig. 3.

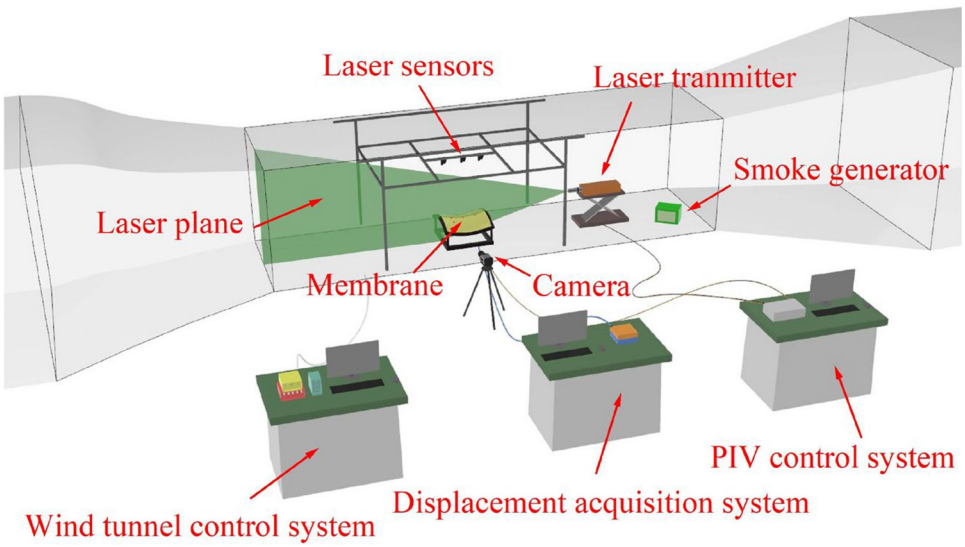

FIG. 3. Schematic diagram of the experiment.

2. Measurement of flow fields

The classic PIV system is used, which consists of a single high-speed camera capturing the fluid velocity in a plan illuminated by a laser light sheet. During the test, the machine oil is heated, and then the tiny particles are formed and released in the tunnel. The space-time evolution of fluid can be identified by the dispersed particles reflecting the light in the laser light sheet. Two reflection flow fields are captured within a short time interval Δt to estimate the velocity field of these particle groups, by using the cross correlation algorithms. To ensure the accurate measurement of fluid dynamics around complex and flexible objects, the precise preliminary calibration should be performed before tests.

The maximum frequency of the dual pulse laser is 1000 Hz, with a pulse energy of up to 20 mJ. The charge-coupled device (CCD) camera possesses a 5 Mega-pixel (i.e., 2160 × 2560) and a maximum sampling frequency of 180 Hz. In this test, the sampling frequency of 60 Hz was used in this study, and the image acquisition frequency was 30 Hz since the image acquisition mode was a dual-frame double exposure. The image field of view was taken in a rectangular shape measuring $80 \times 100\,\text{mm}^2$ (Normal direction × Flow direction). The query window pixels were set to 64 × 64, with an overlap rate of 75%, and the resulting instantaneous velocity field matrix was 2160/64 × 2560/64 = 34 × 40 velocity points, in both flow direction and normal direction. The actual layout diagram is shown in Fig. 4.

3. Measurement of vibration responses

Laser sensors LK-G400 made in Japan were used to monitor displacement response, with an accuracy of 0.05%. In this test, the effective working distance of the laser sensor was 400 mm. Four measurement points for displacements were regularly arranged over the membrane surface, as shown in Fig. 5, to comprehensively analyze the vibration response induced by the separated flow at different locations. The results of point A and point D can analyze the effect of vortex formation and detachment on the membrane, while the results of point B and point C can analyze the characteristics of the structural vibration after the vortex develops sufficiently.

The displacement sensors were installed at a sufficiently elevated position relative to the membrane surface, which would not affect the measurement of the flow field. As shown in Fig. 6 below, it was observed at the experiment site that the trajectory of the tracer particles on the laser plane was not affected by the displacement sensors. A laminar flow region exists between the characteristic turbulent region and the displacement sensors.

According to the scaling criteria, the free stream velocities u_i set as were 5 m/s, 10 m/s, 15 m/s, and 20 m/s, which correspond to the actual wind velocities of 15.81 m/s (near gale), 31.62 m/s (violent storm), 47.43 m/s (typhoon), and 63.25 m/s (strong typhoon). These four grades include all kinds of strong wind conditions that may be encountered in the use of membrane structures. Therefore, the

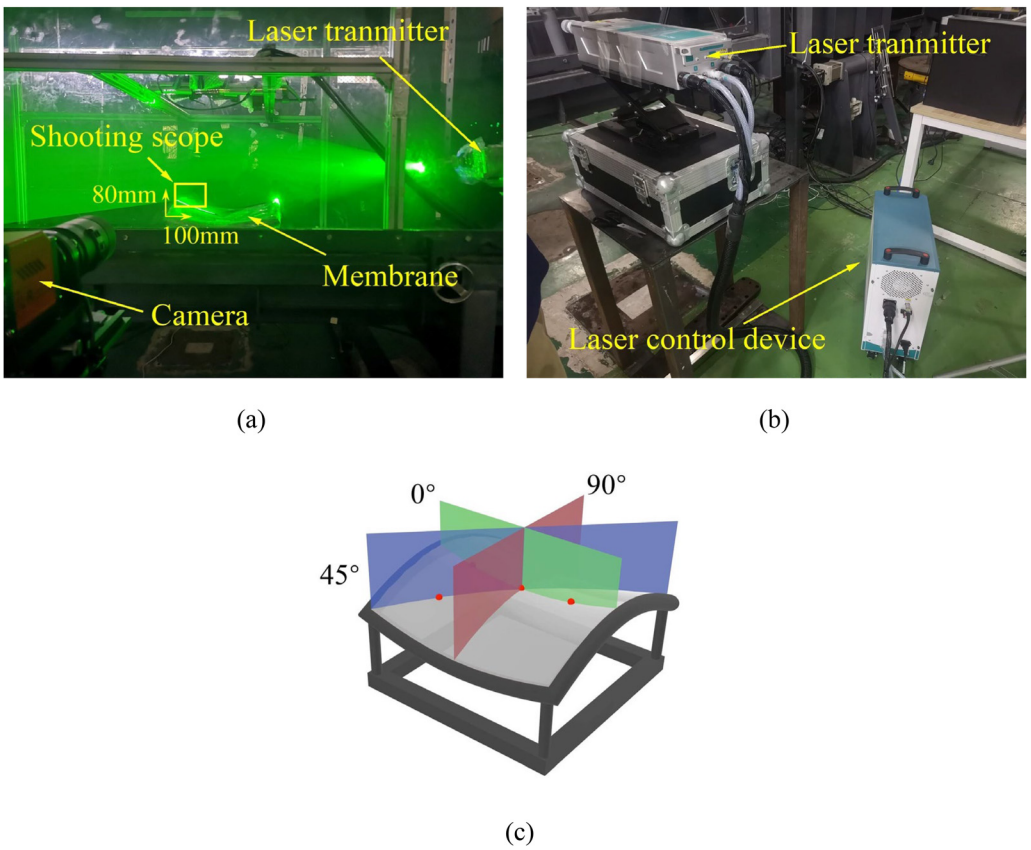

FIG. 4. PIV experiment arrangement: (a) PIV shooting process, (b) photograph of PIV laser transmitter, and (c) PIV laser plane.

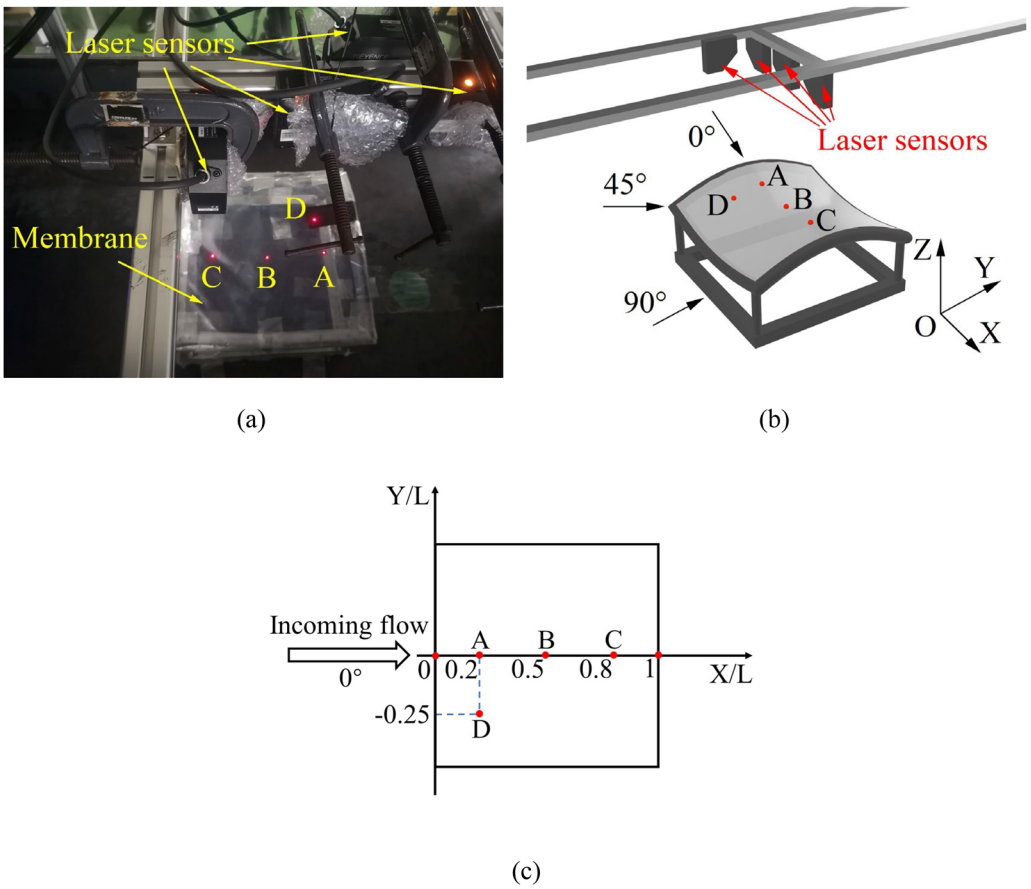

FIG. 5. Schematic diagram and photograph of measurement: (a) photograph of measurement instruments, (b) wind directions and measuring points, and (c) top view of measuring point layout.

Reynolds number of $Re = 1.38 \times 10^5$, 2.76×10^5, 4.14×10^5, 5.52×10^5, respectively in the case of 0° wind direction. The free stream turbulent intensity was less than 0.3% under the current operating conditions. The aeroelastic parameter of $\Pi = (Et/qc)^{1/3}$ has been used by some researchers[9,33,34] to identify the elastic and inertia forces of flexible membrane wings. The parameter of $\Pi_m = (Et/qL)^{1/3}$ was adopted to depict the aeroelastic characteristics of the ETFE membrane. In this equation, E is the modulus of elasticity, t is the

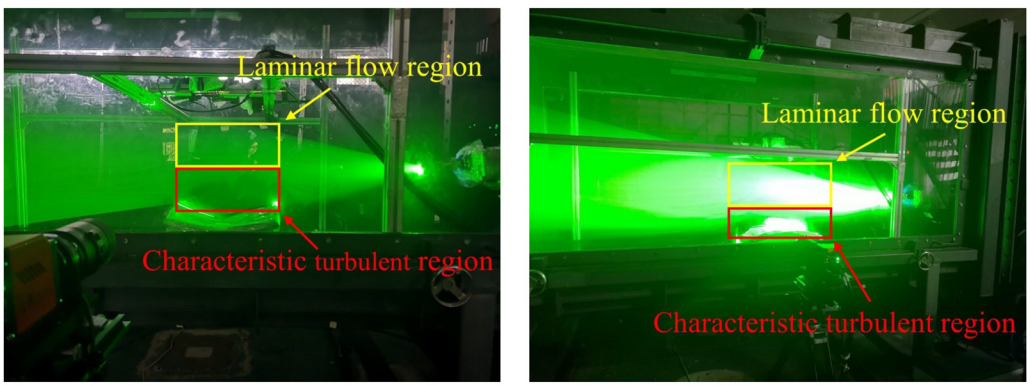

FIG. 6. Photographs of the PIV experiment: (a) 0° wind direction and (b) 90° wind direction.

TABLE III. Summary of testing cases.

Wind direction	Velocity (m/s)			
	5	10	15	20
0°	SSM-5–0	SSM-10–0	SSM-15–0	SSM-20–0
45°	SSM-5–45	SSM-10–45	SSM-15–45	SSM-20–45
90°	SSM-5–90	SSM-10–90	SSM-15–90	SSM-20–90

membrane thickness, L is the span of the membrane and q is the dynamic pressure of the flow, i.e., $q = \rho u_i^2/2$. $\Pi_m = 32.2$, 20.3, 15.5, 12.8 were achieved for $u_i = 5$, 10, 15, 20 m/s, respectively. It should be noted that there is a negative correlation between Π_m and u_i.

The shooting of PIV and the measurement of membrane vibration were carried out concurrently to study the FSI mechanism of membrane structures. Four levels of mean wind velocity (i.e., 5, 10, 15, and 20 m/s) were simulated in the wind tunnel. For each wind field, three approach-flow wind directions were considered including 0°, 45°, and 90°, as shown in Fig. 5(b). A total of 12 testing cases are summarized in Table III.

The testing case ID is named by the tested model, mean wind velocity, and wind direction. For example, the nomenclature of SSM-5–0 means (i) saddle-shaped membrane, (ii) the mean wind velocity is 5 m/s, and (iii) the wind direction is 0°. The sampling frequency of these laser displacement sensors is 1000 Hz. The sampling time in each condition is 65 s when the stationary process of vibration can be formulated.

III. ANALYSIS OF TEST RESULTS

A. Influence of wind directions

Figure 7 shows the streamlines in different wind directions. The Reynolds number for the 90° wind direction cases increases from 1.38×10^5 to 5.52×10^5 as the wind velocity rises from 5 m/s to 20 m/s, which is the same as for the 0° wind. However, the Reynolds number at 45° wind directions based on $\sqrt{2}L$ of $Re = 1.95 \times 10^5$, 3.90×10^5, 5.85×10^5, 7.81×10^5, respectively. The selected PIV view of the flow field is $80 \times 100\ \text{mm}^2$ (vertical axis × horizontal axis). In Fig. 7, the parameter u (instantaneous velocity) is normalized by the parameter u_i (velocity of the incoming flow). The vortex structures at 0° wind direction appear more complex and the development of the vortices is mature. As shown in Fig. 7(a), there are two vortices with different scales. However, in the case of 45° and 90°, the streamlines become smooth, which does not result in any vortex and excites significant vibrations as shown in Figs. 7(b) and 7(c). At the 45° and 90° wind angles, the shape of the membrane surface through which the flow passed is a streamlined body. The flow through the membrane surface is not easy to produce separation and wake. Compared to the 0° angles, the shape of the membrane surface through which the flow passed is a bluff body. The flow separates at the leading edge of the membrane and generates vortices on the membrane surface.

Figure 8 shows the vibration response in different wind directions. As shown in Fig. 8(a), among the three wind directions, the 0° wind direction has the largest mean ($\bar{d}$) and RMS (d_{RMS}) values of 0.584 and 0.0189 mm, respectively. Similarly, as shown in Fig. 8(b), the

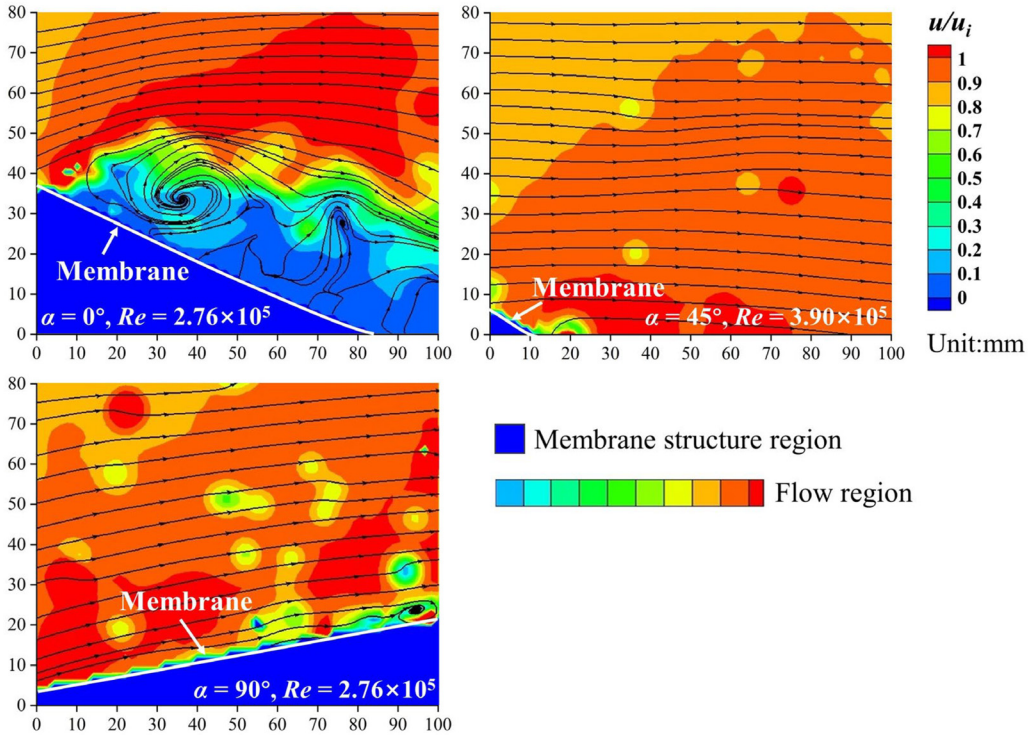

FIG. 7. Streamlines in different wind directions.

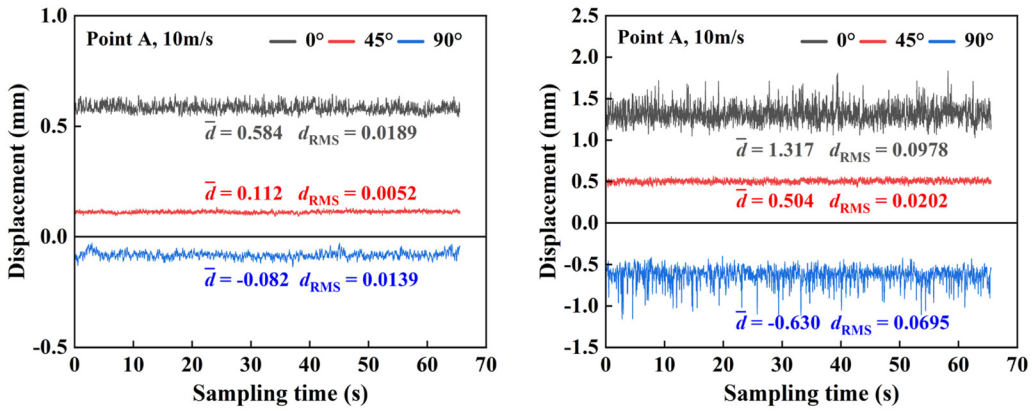

FIG. 8. Vibration response in different wind directions at the wind velocity of 10 m/s: (a) Re = 1.38×10^5 (0° and 90°) or 1.95×10^5 (45°) and (b) Re = 2.76×10^5 (0° and 90°) or 3.90×10^5 (45°).

0° wind direction has the largest mean ($\bar{d}$) and RMS (d_{RMS}) values of 1.317 and 0.0978 mm among the three wind directions, respectively. Compared to 45° and 90° wind directions, the 0° wind direction featured complex vortices, and serious structural vibration responses are more worthy of investigation. To reveal the FSI mechanism of 3D membrane structures, the following part will focus on the case of 0° wind direction.

B. Analysis of flow-induced vibration

1. Displacement-time history

Figure 9 illustrates the displacement time history curves of each point at the Reynolds number of 2.76×10^5. Positive values of displacement statistics indicate suction (i.e., points A and D) while negative values indicate pressure (i.e., points B and C) on the membrane surface. Due to the fact that point A has a larger windward angle than point D, separated flows produce stronger flow fluctuations at point A, causing more prominent vibrations. The vibration response of the membrane exhibits strong randomness and irregularity.

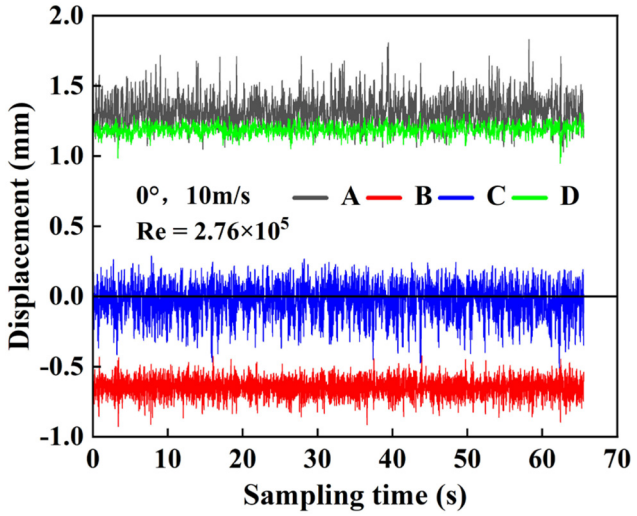

FIG. 9. The displacement time history curves at Re = 2.76×10^5.

2. Normalized mean and RMS values

The normalized mean value of displacement response is defined as $d_m = \bar{d}/t$ while the normalized RMS value of displacement response is defined as $d_r = d_{RMS}/t$, where $\bar{d}$ is the mean value of displacement, d_{RMS} is the RMS value of displacement, and t is the thickness of membrane. Figure 10 shows the mean and RMS values of displacement response (i.e., d_m and d_r). The d_m value at point A exhibits a substantial increase with the growth of Reynolds number, rising from 2.344 to 16.68. Similarly, the d_m value at point D increases from 1.696 to 11.88. However, the d_m value at point B and point C is increasing slightly. The d_m value at point B decreases from −2.514 to −4.254 while the d_m value at the point C decreases from −0.1699 to −3.317. Point A and point D are primarily subjected to the suction influence of the wind, while point B and point C are mainly influenced by the wind pressure, leading to a divergence in their responses. The wind pressure coefficient over four measurement points at $Re = 5.52 \times 10^5$ is shown in Fig. 11. Negative wind pressure coefficients at points A and D indicate the influence of suction. Positive wind pressure coefficients at points B and C indicate the influence of pressure.

Overall, the responses at the leeward side of the membrane (i.e., points A and D) are primarily characterized by an increase in the d_m value, whereas the responses at the windward side of the membrane (i.e., points B and C) are dominated by an increase in the d_r value. This difference arises from the distance between the shear layer and the membrane surface. At the membrane's leading edge, the quasi-static forces prevail, while at the middle to rear sections of the membrane, vortices develop larger and more mature, accentuating the pulsatile effects.

As Fig. 10(b) shown, a progressive rise of the d_r value can be observed at all points. When the wind Reynolds number reaches

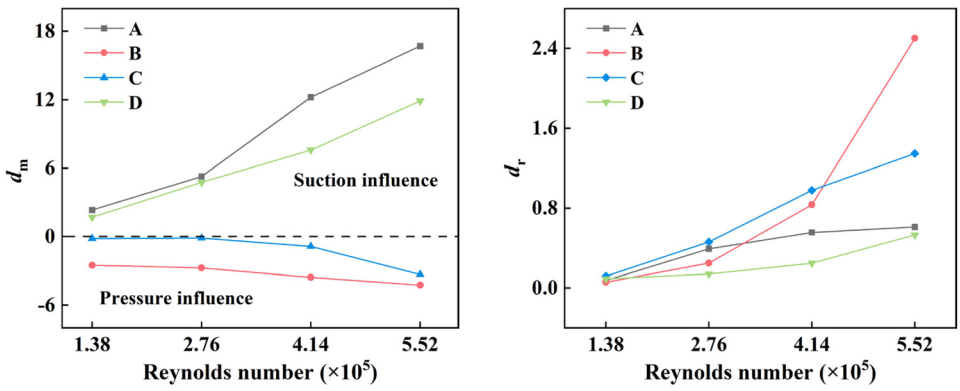

(a) (b)

FIG. 10. The normalized mean and RMS displacement at 0°: (a) normalized mean displacement d_m and (b) normalized RMS displacement d_r.

5.52×10^5, the amplitudes at point B and point C increase faster than those at point A and point D. Especially, the d_r value at point B increases rapidly. It means that at the Reynolds number of 5.52×10^5, the damping of the membrane undergoes a significant decrease, resulting in a substantial increase in amplitudes. The reasons for this trend will be discussed in Sec. IV.

3. Skewness and kurtosis

The probability density functions of the vibration results of point A under four Reynolds numbers are shown in Fig. 12. The normalized displacement is defined as $d_n = d/t$, where d is the measured displacement, and t is the thickness of the membrane. The probability density functions of the vibration response at point A can be fitted by Extreme distribution. As shown in Fig. 12, the probability density functions of the vibration results at the Reynolds number of 1.38×10^5–4.14×10^5 are single-peaked curve, which exhibits slight non-Gaussian properties. The probability density functions of the vibration results at the Reynolds number of 5.52×10^5 is already characterized by a bimodal peak, which exhibits significant non-Gaussian characteristics. When $Re = 1.38 \times 10^5$–2.76×10^5, the skewness value is positive, which shows a left-skewed characteristic, increasing from 0.473 to 0.631. The kurtosis value increases from 2.823 to 4.064, which means the data are more concentrated around the mean displacement value. When $Re = 4.14 \times 10^5$–5.52×10^5, the skewness turns to negative, decreasing from −0.283 to −0.286, showing a right-skewed characteristic. The kurtosis value increases from 3.075 to 3.280, demonstrating that with the Reynolds number rising, the larger turbulence intensity introduces stronger non-Gaussian characteristics. All skewness and kurtosis results at each point are shown in Table IV.

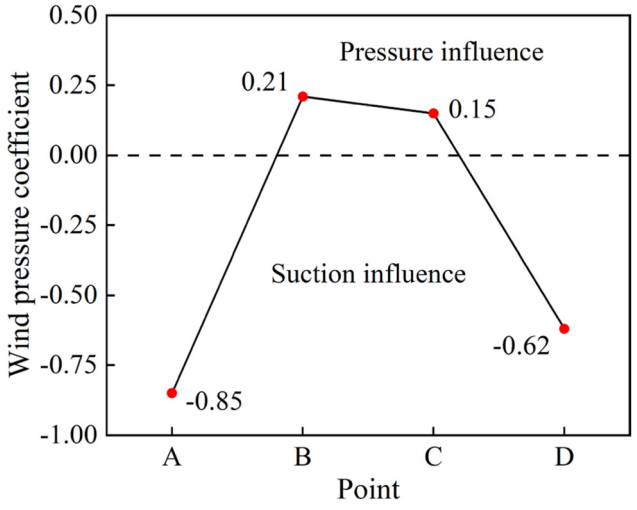

FIG. 11. Wind pressure coefficient over four measurement points at $Re = 5.52 \times 10^5$.

Many studies[19,21,22] on nonlinear theory have mentioned the contribution of nonlinear loads. The probability density of wind pressure also has non-Gaussian characteristics. When the vibrations of the membrane structure exhibit significant non-Gaussian characteristics, as shown in Fig. 13, the wind pressure also displays distinct non-Gaussian features.

C. Analysis of flow characteristics

1. Velocity vector and streamline

In order to compare the flow field under different Reynolds numbers better, the parameter u (instantaneous velocity) is normalized by the parameter u_i (velocity of the incoming flow). Figure 14 shows the normalized instantaneous velocity and the streamline under different Reynolds numbers. The selected PIV view of the flow field is $80 \times 100\,\text{mm}^2$ (vertical axis × horizontal axis). The vortex scale at the same position reduces from 44 to 11 mm as the Reynolds number of the incoming flow increases from 1.38×10^5 to 5.52×10^5. Almost all vortices form from this position and move forward to the end. The increase in Reynolds numbers induces the shear layer closer to the membrane surface, which results in the narrowness of the space where vortices developed and the reduction of vortex scale. The vortices leave the membrane surface and then move forward to the end before they are fully developed. The frequency of vortex shedding may also increase as a result. The vibration responses of the membrane are more significant because of the increasing frequency of external excitation.

Accurately understanding the dynamics of vortex development is fundamental to obtaining the vortex shedding frequency in this

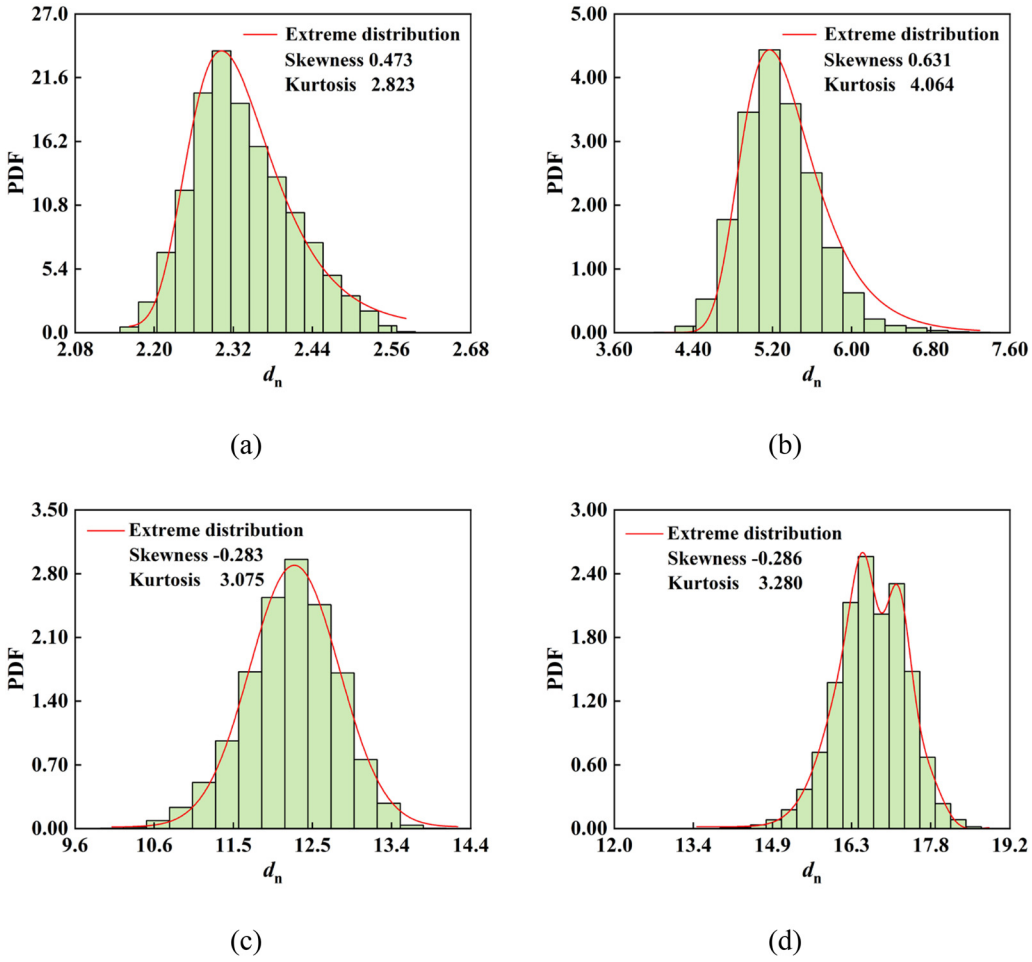

FIG. 12. Probability density function at different Reynolds numbers (at point A at 0°): (a) Re = 1.38×10^5, (b) Re = 2.76×10^5, (c) Re = 4.14×10^5, and (d) Re = 5.52×10^5.

experiment. The development dynamics of vortices is shown in Fig. 15. One cycle of vortex shedding is divided into eight parts. Taking a wind velocity of 20 m/s ($Re = 5.52 \times 10^5$) as an example, the duration of one cycle is 0.404 s, which corresponds to approximately 24.74 Hz.

TABLE IV. Skewness and kurtosis values.

Statistical parameter	Wind velocity (m/s)	Re ($\times 10^5$)	Point A	Point B	Point C	Point D
Skewness	5	1.38	0.473	−0.298	−0.557	−0.876
	10	2.76	0.631	−0.176	−0.422	−0.282
	15	4.14	−0.283	1.791	−0.447	−0.234
	20	5.52	−0.328	0.280	−0.124	−0.439
Kurtosis	5	1.38	−0.177	0.238	0.390	2.166
	10	2.76	1.064	0.213	0.015	1.237
	15	4.14	0.075	4.990	−0.041	1.048
	20	5.52	0.510	−0.284	−0.069	1.159

Figure 16 illustrates the time-averaged velocity cloud map and flow field streamline map at 0° wind direction angle for various Reynolds numbers. The selected PIV view of the flow field is $80 \times 100\ mm^2$ (vertical axis × horizontal axis). The selected period is approximately 3.6 s. As the Reynolds number increases, the shear layer moves closer to the membrane, reducing from 45 mm to 32 mm. When the Reynolds number is 1.38×10^5, only a large vortex K forms near the center of the membrane, with the position of vortex K centered at (93, 32). When the Reynolds number is within the range of 2.76×10^5 to 4.14×10^5, another vortex L begins to emerge at the leading edge of the membrane, which is located at (42, 38) as the Reynolds number is 2.76×10^5 and (38, 37) as the Reynolds number is 4.14×10^5 respectively. As the Reynolds number increases from 2.76×10^5 to 4.14×10^5, the scale of the separated vortex L decreases, the shear layer moves closer to the surface of the membrane, and the position of the vortex core gradually moves forward. When the Reynolds number reaches 5.52×10^5, the vortex L is split into two smaller vortices, resulting in the additional vortex M which is located at (23, 34). The shear layer continues to approach the membrane surface.

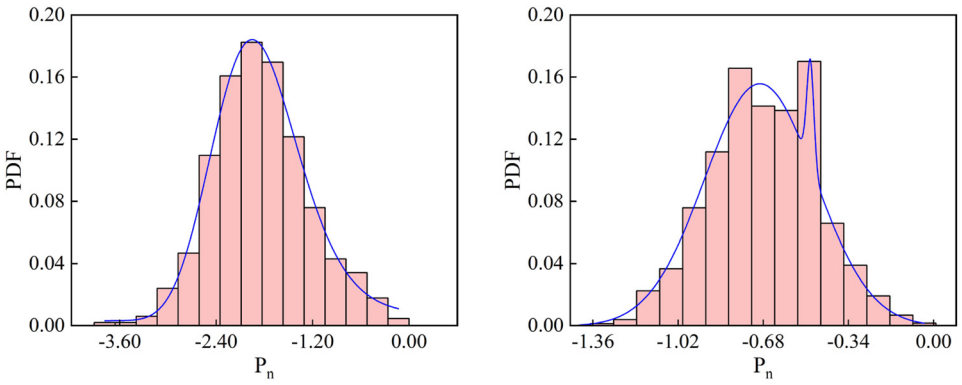

FIG. 13. The PDF of wind pressure: (a) $Re = 4.14 \times 10^5$ and (b) $Re = 5.52 \times 10^5$.

The increased Reynolds number induces the shear layer closer to the surface of the membrane. Meanwhile, the vibration of the membrane excites the shear layer, causing it to rotate and form a series of vortices. As the Reynolds number increases, the number of vortices attached to the membrane surface increases, which induces more contact with the membrane, thus causing more vibrations.

2. Turbulence intensity over membrane surfaces

Figure 17 illustrates the comparison of turbulence intensity $\overline{u'^2 + v'^2}/u_i^2$ as the Reynolds number increases from 1.38×10^5 to 5.52×10^5. The parameter u' represents the horizontal pulsating velocity, while the parameter v' represents the vertical pulsating velocity. The selected PIV view of the flow field is $80 \times 100\,\text{mm}^2$ (vertical axis $\times$ horizontal axis). With the increase in Reynolds number, the large values of turbulence intensity expand in the region. At the Reynolds number of 1.38×10^5, the turbulence intensity is less than 0.3. At the Reynolds number of 2.76×10^5, the turbulence intensity exceeds 0.3 in a small portion. The region where the turbulence intensity surpasses 0.3 becomes larger when the Reynolds number varies from 4.14×10^5 to 5.52×10^5. The strengthened flow fluctuation exacerbates the vibration responses of the membrane.

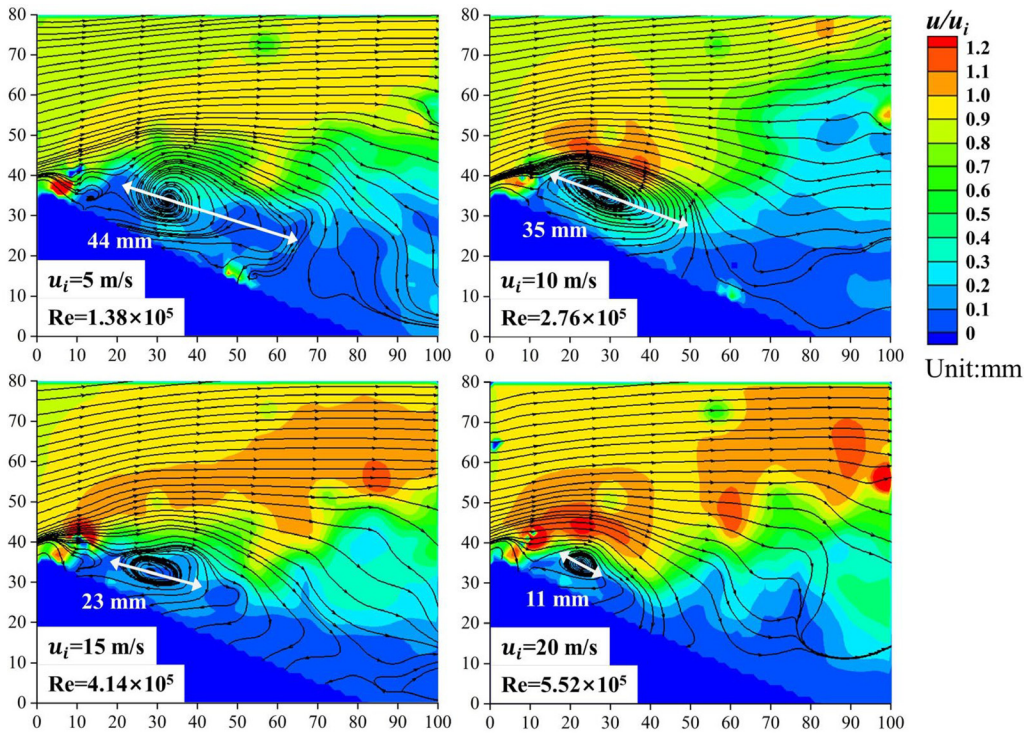

FIG. 14. Normalized instantaneous velocity and streamline at different Reynolds numbers.

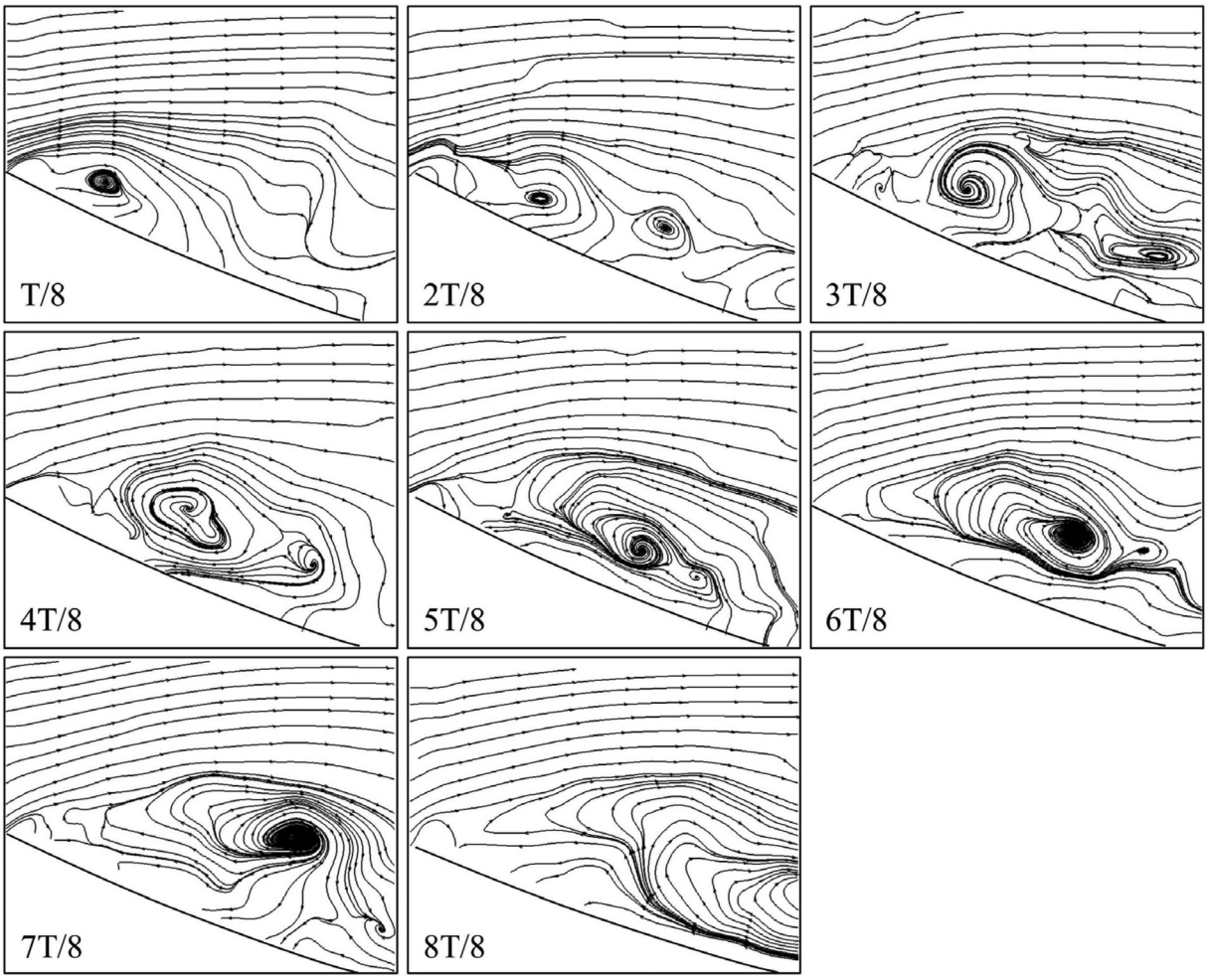

FIG. 15. One cycle of vortex development.

3. Vorticity

Vorticity is one of the important physical quantities used to describe vortex motion. The Ω criterion[35] has the following advantages: it is insensitive to the change of threshold and capable of capturing both strong and weak vortices. $\Omega = 0.5$ means that the antisymmetric tensor is more favorable than the symmetric tensor of the flow. Therefore, Ω slightly larger than 0.5 can be used as the criterion for vortex identification. In this paper, $\Omega = 0.52$ is selected as the threshold value[35] to judge the intersection interface between rotating and non-rotating regions. Figure 18 shows the average vorticity cloud based on the Ω vortex identification criterion. The selected PIV view of the flow field is $80 \times 100\,\text{mm}^2$ (vertical axis × horizontal axis). It can be seen that the Ω criterion is basically accurate for vortex identification in this experiment. According to the average vorticity, the vortex density A_v/A and the number of vortices varying with the Reynolds number can be obtained, as shown in Fig. 19. The parameter A_v is the total area of the vortices, while the parameter $A = 8 \times 10^3\,\text{mm}^2$. As the Reynolds number increases, the density of vortices decreases from 5.46% to 3.01%, while the number of vortices increases from 1 to 3. As the shear layer approaches the membrane surface, the number of vortices and vortex intensity increase, even though the vortex size and density of vortices decrease. This phenomenon means that strong vortices act on the membrane surface and then intensify the vibrations of the membrane.

D. POD modes decomposition

By utilizing the POD method,[36–39] the flow field data obtained by PIV can be decomposed into different modes. Component P refers to the positive vortex which is rotating counterclockwise, and N refers to the negative vortex which is rotating clockwise, as shown in Fig. 20. In the first five modes of the flow field, the forms of vortex shedding can be categorized into three types. Component S represents the pattern of single vortex shedding (i.e., 1st mode), D represents the pattern of paired vortex shedding (i.e., second to fourth mode), and S + D represents the pattern of single vortex shedding and paired vortex shedding alternately (i.e., fifth mode).

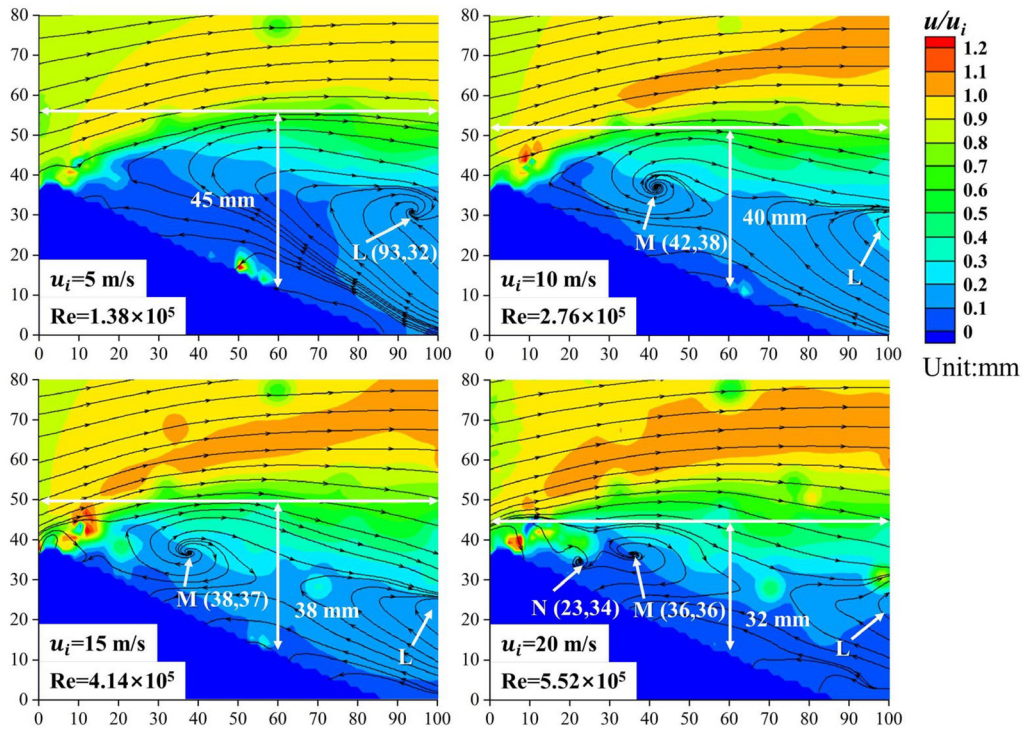

FIG. 16. Normalized time-averaged velocity and streamline at different Reynolds numbers.

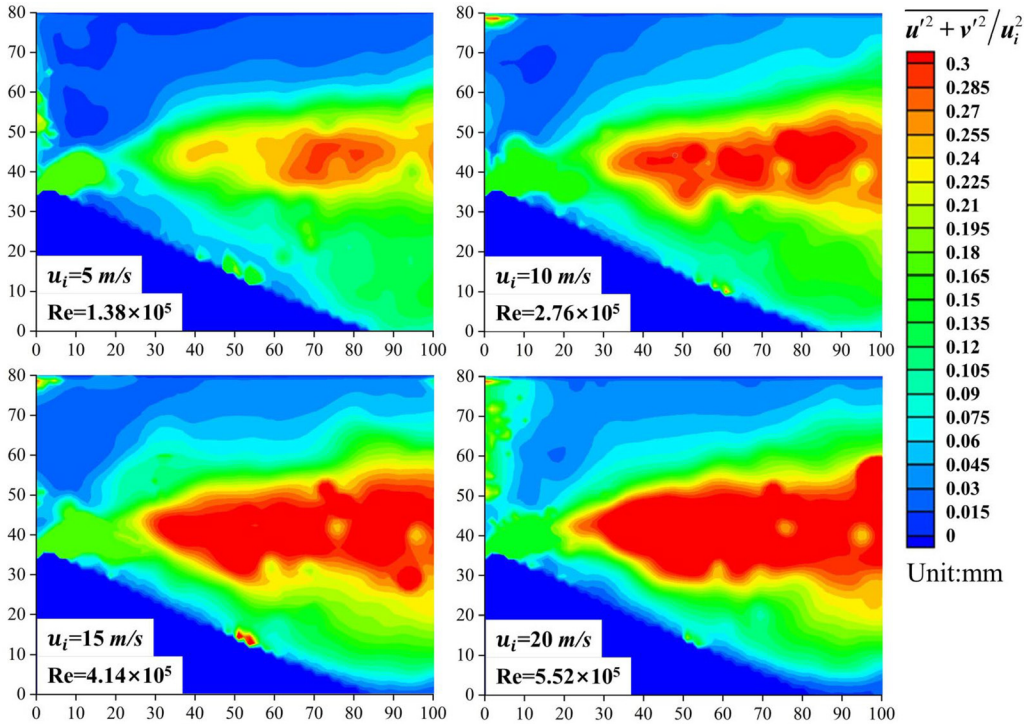

FIG. 17. Turbulence intensity at different Reynolds numbers.

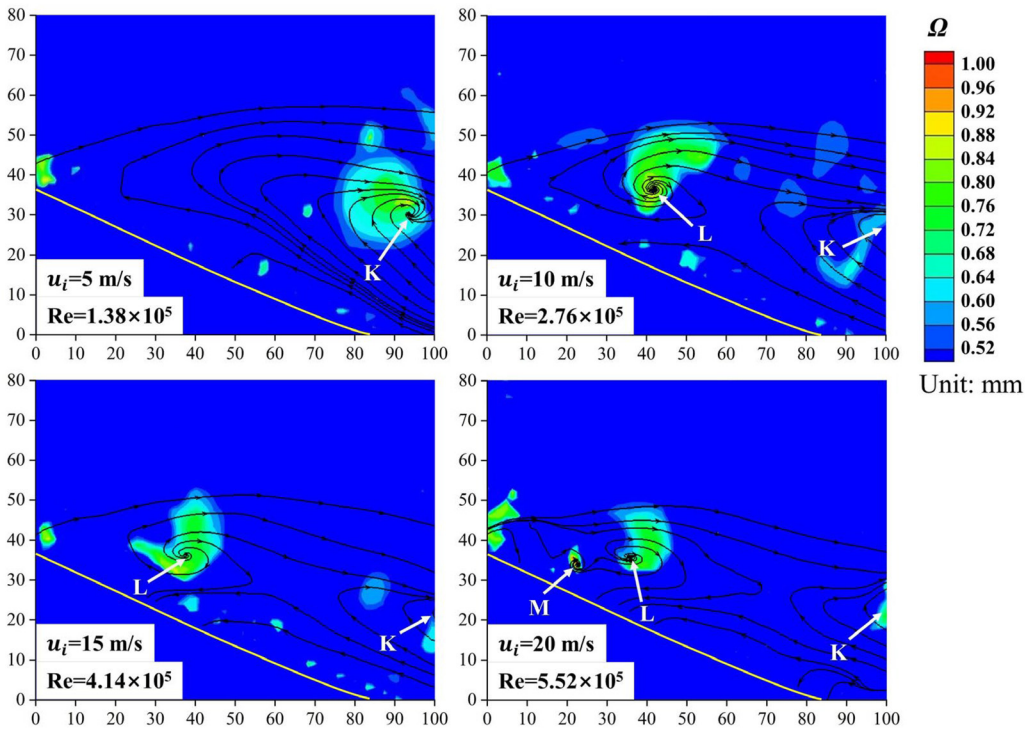

FIG. 18. Vorticity at different Reynolds numbers.

The first five modes of POD decomposition have different features. The first mode extracted from the flow field only has a positive vortex located near the front separation point of the flow field. The second mode is divided into two opposite vortices, with the positive vortex located above and the negative vortex below, while the third mode is a pattern of alternating shedding of a positive and a negative vortex. Then, the shedding form of vortices in the fourth mode is two positive vortices followed by two negative vortices, and the shedding form of vortices in the fifth mode is one positive vortex followed by two negative vortices.

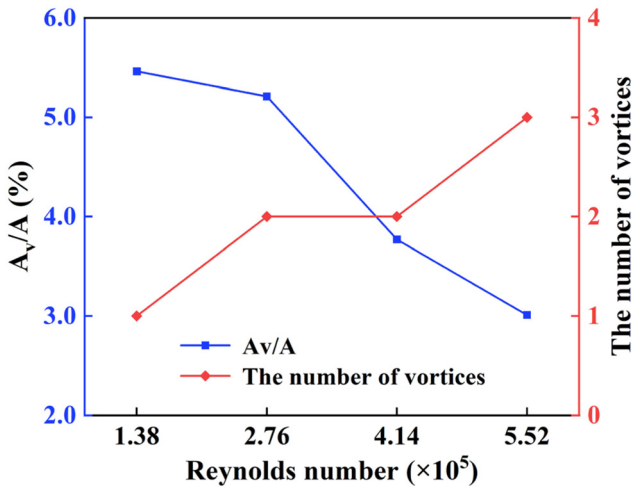

FIG. 19. Vortex density and the number of vortices at different Reynolds numbers.

The POD decomposition not only reveals the vortex shedding modes shown in Fig. 20 but also provides the corresponding eigenvalues and energy contributions for each mode as shown in Fig. 21. Figure 21(a) displays the energy proportion of the first twenty POD modes, where λ_n is the eigenvalue corresponding to a certain mode, lg (λ_n) represents the logarithmic eigenvalues and n denotes the mode order. It can be observed that the first five modes account for the vast majority of energy in the flow field under different Reynolds numbers. The curve rapidly decreases from the first to the second mode, with λ_n decaying quickly, indicating the dominance of the 1st POD mode. In order to analyze the energy proportion of the first five POD modes under different Reynolds numbers, the energy proportion curves are plotted, as shown in Fig. 21(b). The energy proportion of the 1st mode exceeds 50% in all test cases, while the energy proportion of modes second to fifth is below 5%. With increasing Reynolds number, the energy proportion of the first mode continuously decreases from 94.88% to 53.95%. As the Reynolds number increases, the energy proportion of the higher-order modes demonstrates a progressive increase, with the largest energy proportion up to 4.63%. This elevation in the energy contribution of higher-order modes signifies an escalating complexity in the flow field, facilitating more energy transfer to the membrane structure and intensifying the vibrations of the membrane structure.

IV. FSI MECHANISM DISCUSSIONS

In order to reveal the fluid–solid interaction of membrane structures in laminar flows, both the shear layer and the displacement response are analyzed for each instantaneous flow. Figure 22 illustrates

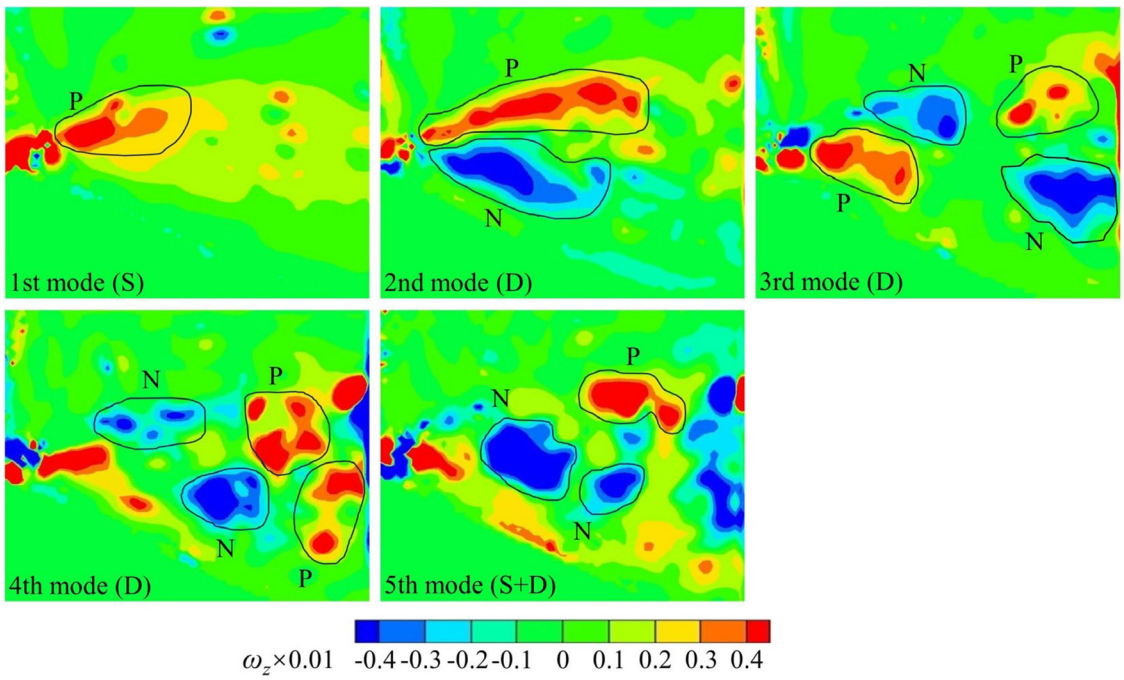

FIG. 20. POD modes.

the correlation between the flow field and membrane vibration at the Reynolds number of 4.14×10^5. Figure 22(a) shows the minimum displacement and maximum displacement at point A from the shooting scope of the PIV camera (i.e., minimum displacement A_1 and maximum displacement A_2). Figure 22(b) shows the displacement history result as point A. In Fig. 22(b), t_1 represents the time when point A moved to the lowest point position of A_1, while t_2 represents the time when point A moved to the highest point position of A_2. At the moment of t_1, the corresponding flow field is shown in Fig. 22(c), while the corresponding flow field at the moment of t_2 is depicted in Fig. 22(d). Specifically, the vortex scale is larger, the vortex core is positioned higher, and the shear layer is further away from the membrane surface at the position of A_2 compared to the position of A_1, which has been mentioned in literature.[9] This phenomenon is attributed by the oscillation of the membrane, which induces variations of flows in space between the shear layer and the membrane surface. On the other hand, vortices approaching closer to the membrane surface will exert stronger vortex-induced forces, leading to the larger vibration response of the membrane.

By analyzing the membrane structural response, the structural parameters can be determined through the Bayesian fast Fourier transform (FFT) method. Figure 23 illustrates the power spectral density

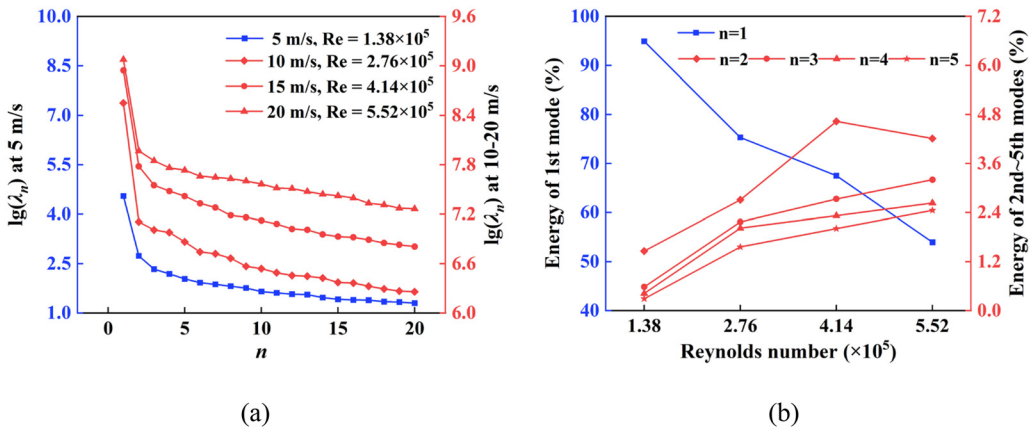

FIG. 21. Flow field decomposition results by POD method: (a) the logarithmic eigenvalues lg(λ_n) and (b) energy proportion of modes.

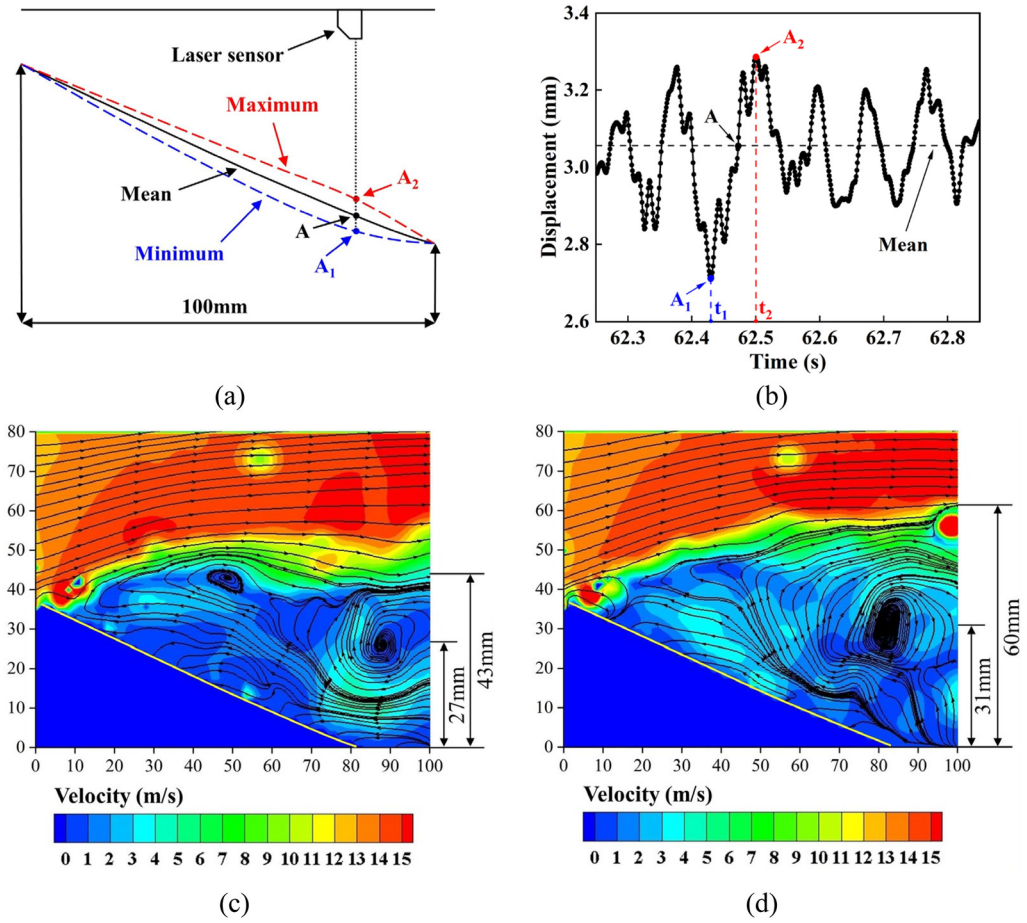

FIG. 22. Comparison of the flow field above point A at the Reynolds number of 4.14×10^5: (a) displacement of point A, (b) displacement-time of point A, (c) flow field at lowest displacement (A_1), and (d) flow field at highest displacement (A_2).

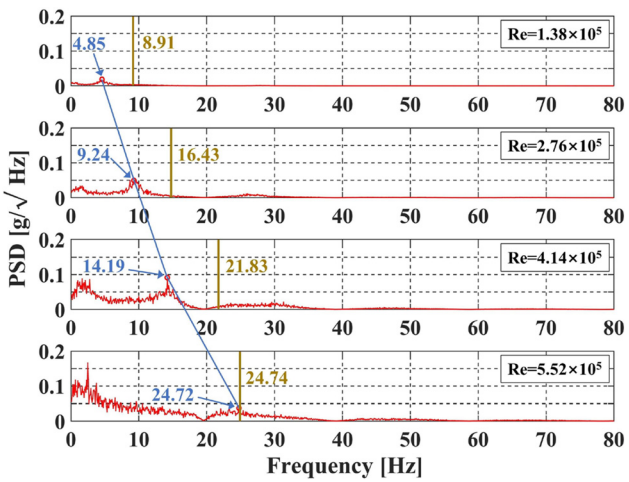

FIG. 23. PSD of displacement and wind speed at different Reynolds numbers.

(PSD) of the displacements under various Reynolds numbers. In the PSD curves for all wind Reynolds numbers, the leftmost peak is associated with the background response. The vortex shedding frequency f_v in the wind spectrum (marked by an orange line) and the fundamental frequency of structures f_s (marked by a blue line) are shown in Fig. 23. The structural frequency f_s varying with Reynolds numbers shows a nonlinear trend, increasing from 4.85 to 24.72 Hz when the Reynolds number increases from 1.38×10^5 to 5.52×10^5. The vortex shedding frequency f_v (i.e., 24.74 Hz) is ultimately matched with the structural frequency f_s (i.e., 24.72 Hz) at the Reynolds number of 5.52×10^5, with the occurrence of lock-in phenomenon.

In these literatures,[18,28,31,32] the vibration frequency of closed membrane structures[18,31] or membrane structures with tension[28,32] is almost unchanged under different wind velocities. The internal pressure of the closed membrane and the tension of the membrane significantly reduce the impact of wind pressure on the stiffness of membrane structures, so that the vibration frequency of these membrane structures remains almost unchanged. However, in this paper, the identified structural natural frequencies increase as the Reynolds

number increases, as shown in Fig. 23. This phenomenon is attributed by the elastically mounted boundary condition. The membrane exhibited minimal tension with its structural form-finding and attachment with the steel frame. However, aerodynamic forces induced a transition in the membrane from a state of minimal tension to a state of larger tension. That was due to the fact that the increased Reynolds number resulted in a pressure difference between the upper and lower membrane surfaces. In order to maintain the balance in forces, the increased pressure difference was balanced by increased membrane tension. The increasing tension over the membrane surface would lead to an improvement in structural stiffness and vibration frequency, and ultimately the vibrations of the membrane would shift from linear type to nonlinear type. The similar phenomena can be found in the relative researches.[29,30,40,41]

According to the methods in these researches,[42–45] the damping ratios of each order and the contribution of each order responses to the total responses can be obtained. The damping ratios of each order of the membrane are evaluated using bandpass filtering and an improved random decrement technique (RDT). The total damping ratio ξ_t is the weighted average of the damping ratios of each order of the membrane. The damping ratio of the membrane structure is measured to be 1.5% before the wind tunnel tests.

As shown in Fig. 24, the total damping ratio ξ_t of the structure decreases from 6.04% to 0.49% as the Reynolds number increases from 1.38×10^5 to 5.52×10^5. This indicates that the aerodynamic damping ratio ξ_a of the structure reduces to negative (i.e., −1.03%) at the Reynolds number of 5.52×10^5, as shown in Fig. 24.

Within the range of Reynolds number from 1.38×10^5 to 4.14×10^5, the analytical results reveal that the vortex shedding frequency f_v and the fundamental membrane vibration frequency f_s do not overlap, indicating the absence of conditions which is conducive to vortex-induced vibration (VIV). In addition to the above frequency results, based on the single-peak probability density functions in Fig. 12 and the positive values of aerodynamic damping ratio ξ_a in Fig. 24, the vibration responses of the membrane are identified as turbulent buffeting[31,46,47] as the Reynolds number increases from 1.38×10^5 to 4.14×10^5. However, there are three factors indicate that the vibration of the membrane structures will shift from turbulent buffeting to vortex-induced vibration (VIV) as the Reynolds number increases: (I) The pronounced upward in normalized RMS values depicted in Fig. 10. (II) The frequency f_s and the frequency f_v gradually overlapped as shown in Fig. 23. (III) The aerodynamic damping ratio ξ_a of the structure decreased to negative at the Reynolds number of 5.52×10^5, which is illustrated in Fig. 24.

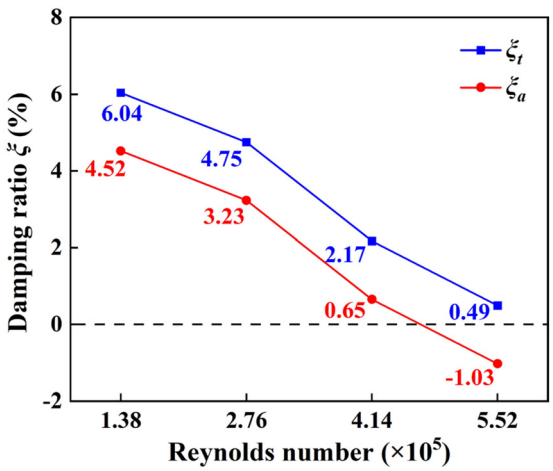

FIG. 24. Damping ratios at different Reynolds numbers.

V. CONCLUSIONS

This study experimentally investigates the fluid–solid interaction mechanism of the saddle-shaped membrane structure under laminar flows, combining the flow field characteristics with wind-induced responses. The evolution in the wind field is visualized by using the PIV technique. The aerodynamic characteristics of the membrane structure including vibration statistics, frequency, and damping ratio are measured and analyzed in detail. The main conclusions are summarized as follows:

(1) The 0° wind direction is the most unfavorable wind direction, with two significant features. (I) The vortices develop more fully and maturely, resulting in the higher characteristic turbulence intensity. (II) The structural dynamic response becomes more significant, increasing more risks of aero-instability and failure. From the view of statistics, the normalized mean and RMS values of displacement responses nonlinearly increase with the increasing Reynolds number.

(2) The shear layer may closely approach the membrane surface in larger wind Reynolds number cases, which would hinder the evolution of vortices. Resultantly, the vortices turn out smaller in scale and closer in space, which further increases the frequency of vortex shedding, stronger FSI effect, and potential vortex-induced resonance.

(3) The forms of vortex shedding can be decomposed in the first five modes, and divided into three patterns: (I) the single vortex shedding (i.e., first), (II) the paired alternating vortex shedding (i.e., second to fourth), and (III) the single vortex shedding conjoined with paired alternating vortex shedding (i.e., fifth). The first mode plays a dominant role in the composition of the flow field, although the higher-order complex modes participate more with the increasing wind speed.

(4) As the *Re* increases from 1.38×10^5 to 5.52×10^5, the vibration frequency f_s rises from 4.85 to 24.72 Hz. Compared to closed and tensioned membrane structures, membranes with elastically mounted boundary conditions are more susceptible to surface wind pressures that can change stiffness. Therefore, in practical applications, attention should be paid to the FSI effects of the membrane structures, which has elastically mounted boundary conditions.

(5) When the vortex shedding frequency f_v is approaching the fundamental frequency of the membrane structure f_s at the Reynolds number of 5.52×10^5, the turbulent buffeting would turn into the vortex-induced resonance, featured with lock-in frequency, significant amplified displacement, and negative aerodynamic damping ratio.

ACKNOWLEDGMENTS

This study has been financially supported by the National Natural Science Foundation of China (Grant No. 52108121), the

China Postdoctoral Science Foundation Funded Project (Grant No. 2024M753652), the Open Research Subject of Key Laboratory of Fluid and Power Machinery (Xihua University), and the Ministry of Education (Grant No. LTDL-2023019).

AUTHOR DECLARATIONS

Conflict of Interest

The authors declare that there are no conflicts of interest.

Author Contributions

Dong Li: Funding acquisition (equal); Methodology (equal); Project administration (equal). **Renyang Shen:** Software (equal); Writing—original draft (equal). **Qiyin Zhu:** Software (equal); Visualization (equal). **Leiyu Lu:** Data curation (equal); Writing—original draft (equal). **Hao Ding:** Writing—review & editing (equal). **Xiaoqiang Yang:** Conceptualization (equal); Writing—review & editing (equal).

DATA AVAILABILITY

The data that support the findings of this study are available from the corresponding author upon reasonable request.

REFERENCES

[1]A. Michalski, B. Gawenat, P. Gelenne, E. Haug, R. Lohner, R. Wuchner, and K. Bletzinger, "Validation of the computational fluid–structure interaction simulation at real-scale tests of a flexible 29 m umbrella in natural wind flow," J. Wind Eng. Ind. Aerodyn. **99**(4), 400–413 (2011).
[2]Y. Yin, W. Chen, J. Hu, B. Zhao, and Q. Wang, "In-situ measurement of structural performance of large-span air-supported dome under wind loads," Thin-Walled Struct. **169**, 108476 (2021).
[3]D. Li, Z. Lai, C. Liu, J. Guo, X. Yang, and M. Guan, "Random vibration of pretensioned rectangular membrane structures under heavy rainfall excitation," Thin-Walled Struct. **164**, 107856 (2021).
[4]Y. Yu and Y. Liu, "Flapping dynamics of a piezoelectric membrane behind a circular cylinder," J. Fluids Struct. **55**, 347–363 (2015).
[5]Y. Yu, Y. Liu, and X. Amandolese, "A review on fluid-induced flag vibrations," Appl. Mech. Rev. **71**(1), 010801 (2019).
[6]E. Kimoto and S. Kawamura, "Aerodynamic behaviour of one-way type hanging roofs," J. Wind Eng. Ind. Aerodyn. **13**(1), 395–405 (1983).
[7]T. Ohkuma and H. Marukawa, "Mechanism of aeroelastically unstable vibration of large span roof," J. Wind Eng. Ind. Aerodyn. **1990**, 35–42.
[8]A. Miyake, T. Yoshimura, and M. Makino, "Aerodynamic instability of suspended roof models," J. Wind Eng. Ind. Aerodyn. **42**(1), 1471–1482 (1992).
[9]P. Rojratsirikul, Z. Wang, and I. Gursul, "Unsteady fluid–structure interactions of membrane airfoils at low Reynolds numbers," Exp. Fluids **46**(5), 859–872 (2009).
[10]L. Tregidgo, Z. Wang, and I. Gursul, "Unsteady fluid–structure interactions of a pitching membrane wing," Aero. Sci. Technol. **28**, 79–90 (2013).
[11]H. Demir and M. Genç, "An experimental investigation of laminar separation bubble formation on flexible membrane wing," Eur. J. Mech B/Fluids. **65**, 326–338 (2017).
[12]M. Genç, H. Demir, M. Özden, and T. Bodur, "Experimental analysis of fluid–structure interaction in flexible wings at low Reynolds number flows," Aircr. Eng. Aerosp. Technol. **93**(6), 1060–1075 (2021).
[13]Z. Yu, Y. Zhou, Y. Li, and A. Yoshida, "Effect of added mass on wind-induced vibration of a circular flat membrane by wind tunnel tests," Int. J. Struct. Stab. Dyn. **18**(12), 22 (2018).
[14]R. Gordnier, "High fidelity computational simulation of a membrane wing airfoil," J Fluids Struct. **25**(5), 897–917 (2009).
[15]T. Li, Q. Yang, and T. Ishihara, "Unsteady aerodynamic characteristics of long-span roofs under forced excitation," J. Wind Eng. Ind. Aerodyn. **181**, 46–50 (2018).
[16]Y. Takadate and Y. Uematsu, "Steady and unsteady aerodynamic forces on a long-span membrane structure," J. Wind Eng. Ind. Aerodyn. **193**, 103946–103946 (2019).
[17]Q. Yang, F. Chen, B. Yan, T. Li, and J. Yan, "A transport model of convective flow on self-excited vibrating flat flexible roofs using LES," J. Wind Eng. Ind. Aerodyn. **238**, 105426 (2023).
[18]Q. Yang, F. Chen, Y. Tamura, T. Li, and B. Yan, "Fluid–structure interaction behaviors of tension membrane roofs by fully-coupled numerical simulation," J. Wind Eng. Ind. Aerodyn. **244**, 105609 (2024).
[19]C. Liu, M. Wang, and Z. Zheng, "Nonlinear wind-induced aerodynamic stability of orthotropic saddle membrane structures," J. Wind Eng. Ind. Aerodyn. **164**, 119–127 (2017).
[20]S. Rasim and M. Senad, "Nonlinear analysis of hyperelastic membrane," in Advanced Technologies, Systems, and Applications II: Proceedings of the International Symposium on Innovative and Interdisciplinary Applications of Advanced Technologies (IAT), Lecture Notes in Networks and Systems (Springer, Cham, 2018), Vol. 28, pp. 661–670.
[21]T. Wang, K. Guo, Q. Yang, and B. Cheng, "Estimation of wind-induced response of large membrane structures with nonlinear motion-induced aerodynamic force and nonlinear geometric stiffness," J. Wind Eng. Ind. Aerodyn. **235**, 105356 (2023).
[22]C. Liu, R. Pan, X. Deng, H. Xie, J. Liu, and X. Wang, "Random vibration and structural reliability of composite hyperbolic–parabolic membrane structures under wind load," Thin-Walled Struct. **180**, 109878 (2022).
[23]M. Glück, M. Breuer, F. Durst, A. Halfmann, and E. Rank, "Computation of wind-induced vibrations of flexible shells and membranous structures," J. Fluid Struct. **17**, 739–765 (2003).
[24]M. Alexander, G. Bernhard, G. Philippe, and H. Eberhard, "Computational wind engineering of large umbrella structures," J. Wind Eng. Ind. Aerodyn. **144**, 96–107 (2015).
[25]X. Wang, H. Chu, and Q. Yang, "Numerical analysis of wind-induced response of a wrinkled membrane," Int. J. Struct. Stab. Dyn. **20**(05), 24 (2020).
[26]Q. Yang, T. Wang, B. Yan, T. Li, and M. Liu, "Nonlinear motion-induced aerodynamic forces on large hyperbolic paraboloid roofs using LES," J. Wind Eng. Ind. Aerodyn. **216**, 104703 (2021).
[27]A. Kandel, X. Sun, and Y. Wu, "Wind tunnel experiment on rectangular-shaped arch-supported membrane structures," Structures **41**, 1515–1531 (2022).
[28]D. Li, Z. Zhang, C. Zhang, Z. Zhang, and X. Yang, "Aeroelastic experimental investigation of hyperbolic paraboloid membrane structures in normal and typhoon winds," Sustainability **14**(19), 12207–12207 (2022).
[29]C. Liu, M. Wang, X. Deng, D. Li, J. Liu, and X. Wang, "Impact of saddle membrane structure by hail with combined particle sizes: Numerical simulation and experimental investigation," Eng. Struct. **264**, 114477 (2022).
[30]J. Wood, M. Breuer, and G. Nayer, "Experimental studies on the instantaneous fluid–structure interaction of an air-inflated flexible membrane in turbulent flow," J. Fluids Struct. **80**, 405–440 (2018).
[31]Y. Wu, K. Yan, and Z. Chen, "Aeroelastic wind tunnel investigations on rectangular-planed air-supported membrane structures," Thin-Walled Struct. **190**, 110955 (2023).
[32]D. Li, Q. Zhu, R. Shen, L. Lu, and Z. Lai, "Random vibration response and reliability analysis of hyperbolic parabolic membrane structures under typhoons," Thin-Walled Struct. **205**, 112444 (2024).
[33]R. Smith and W. Shyy, "Computation of aerodynamic coefficients for a flexible membrane airfoil in turbulent flow: A comparison with classical theory," Phys Fluids **8**(12), 3346–3353 (1996).
[34]X. He, Q. Guo, and J. Wang, "Regularities between kinematic and aerodynamic characteristics of flexible membrane wing," Chin. J. Aeronaut. **35**(11), 209–218 (2022).
[35]C. Liu, Y. Wang, Y. Yang, and Z. Duan, "New omega vortex identification method," Sci. China **59**(08), 62–70 (2016).
[36]R. Padilla, V. Durgesh, T. Xing, and A. Nawafleh, "Experimental study of flag fluid–structure interaction in a laminar jet and application of POD," J. Fluids Struct. **125**, 104040 (2024).
[37]T. Lang, H. Wang, Z. Liu, Z. Xu, and H. Gao, "Vortex-induced vibration performance and mechanism analysis of a suspension bridge affected by water-filled barriers," Int. J. Struct. Stab. Dyn. **24**(16), 2450180 (2023).

[38]G. Riches, R. Martinuzzi, and C. Morton, "Proper orthogonal decomposition analysis of a circular cylinder undergoing vortex-induced vibrations," Phys. Fluids **30**, 105103 (2018).
[39]J. Ribeiro and W. Wolf, "Identification of coherent structures in the flow past a NACA0012 airfoil via proper orthogonal decomposition," Phys. Fluids **29**, 085104 (2017).
[40]D. Tang and E. Dowell, "Experimental aerodynamic response for an oscillating airfoil in buffeting flow," AIAA J. **52**(6), 1170–1179 (2014).
[41]F. Sun, H. Tang, M. Lu, D. Zhang, and C. Lu, "A study on wind pressure characteristics of a large-span membrane structure under the fluctuating wind in a vertical direction based on a large eddy simulation," Mod. Simul. Eng. **2022**, 8209487.
[42]Y. Tamura and S. Suganuma, "Evaluation of amplitude-dependent damping and natural frequency of buildings during strong winds," J. Wind Eng. Ind. Aerodyn. **59**(2/3), 115–130 (1996).
[43]H. Marukawa, N. Kato, K. Fujii, and Y. Tamura, "Experimental evaluation of aerodynamic damping of tall buildings," J. Wind Eng. Ind. Aerodyn. **59**(2/3), 177–190 (1996).
[44]A. Kareem and K. Gurley, "Damping in structures: Its evaluation and treatment of uncertainty," J. Wind Eng. Ind. Aerodyn. **59**(2/3), 131–157 (1996).
[45]Y. Wu, Z. Chen, and X. Sun, "Research on the wind-induced aero-elastic response of closed-type saddle-shaped tensioned membrane models," J. Zhejiang Univ. Sci. A **16**(8), 656–668 (2015).
[46]S. Jorge, C. Andrea, and C. Felipe, "Experimental investigation on the role of turbulent buffeting on the dynamics of a flexible filament in airflow," Exp. Therm Fluid Sci. **149**, 111011 (2023).
[47]A. Mayori and D. Rockwell, "Interaction of a streamwise vortex with a thin plate—A source of turbulent buffeting," AIAA J. **32**, 2022 (2012).